Large-Eddy Simulation of the Stable Boundary Layer with Explicit Filtering and Reconstruction Turbulence Modeling

BOWEN ZHOU AND FOTINI KATOPODES CHOW

Civil and Environmental Engineering, University of California, Berkeley, Berkeley, California

(Manuscript received 7 October 2010, in final form 11 April 2011)

ABSTRACT

Large-eddy simulation (LES) of the stably stratified atmospheric boundary layer is performed using an explicit filtering and reconstruction approach with a finite difference method. Turbulent stresses are split into the resolvable subfilter-scale and subgrid-scale stresses. The former are recovered from a reconstruction approach, and the latter are represented by a dynamic eddy-viscosity model. The resulting dynamic reconstruction model (DRM) can sustain resolved turbulence with less stringent resolution requirements than conventional closure models, even under strong atmospheric stability. This is achieved by proper representation of subfilter-scale (SFS) backscatter of turbulent kinetic energy (TKE). The flow structure and turbulence statistics for the moderately stable boundary layer (SBL) are analyzed with high-resolution simulations. The DRM simulations show good agreement with established empirical formulations such as flux and gradient-based surface similarity, even at relatively coarse resolution. Similar results can be obtained with traditional closure models at the cost of higher resolution. SBL turbulence under strong stability is also explored. Simulations show an intermittent presence of elevated TKE below the low-level jet. Overall, the explicit filtering and reconstruction approach is advantageous for simulations of the SBL. At coarse resolution, it can extend the working range of LES to stronger stability, while maintaining agreement to similarity theory; at fine resolution, good agreement with theoretical formulations provides confidence in the results and allows for detailed investigation of the flow structure under moderate to strong stability conditions.

1. Introduction

Turbulent motions in the stably stratified atmospheric boundary layer are limited by the buoyancy length scale, thus requiring much higher grid resolution in numerical simulations than for neutral or convective conditions. Large-eddy simulation (LES) can be used to resolve turbulent flows in the stable boundary layer (SBL) because it is based on the definition of a spatial filter that can be adjusted to resolve necessary flow features. The spatial filter separates the large resolved scales from the subfilter-scale (SFS) motions. The effect of subfiltered motions on the resolved scales must be represented with a turbulence model.

LES of the SBL has been performed mostly under idealized conditions and is limited to weak or moderate stability with conditions of either high geostrophic forcing or a low surface cooling rate (Saiki et al. 2000; Kosovic and Curry 2000; Basu and Porté-Agel 2006). The need for high grid resolution is the primary constraint for extending the application of LES to strongly stable conditions. Over real complex terrain, performing LES of nighttime atmospheric flow is more challenging because the available spatial resolution for mesoscale simulations is even more limited. Given these constraints, the SFS representation of turbulence, that is, the LES turbulence closure model, becomes crucial for SBL simulations. Various turbulence models have emerged in the quest of accurately simulating SBL turbulence, for example, the nonlinear model (Kosovic and Curry 2000), the scale-dependent dynamic model (Basu and Porté-Agel 2006), and the turbulent kinetic energy–based model (Jiménez and Cuxart 2005). The performance of many existing models with a moderate SBL can be found in the Global Energy and Water Cycle Experiment (GEWEX) Atmospheric Boundary Layer Study (GABLS) LES intercomparison studies (Beare et al. 2006).

To perform LES of a turbulent SBL, the closure model must be able to sustain resolved turbulence,

Corresponding author address: Fotini Chow, Dept. of Civil and Environmental Engineering, University of California, Berkeley, Berkeley, CA 94720-1710.
E-mail: tinakc@berkeley.edu

DOI: 10.1175/2011JAS3693.1

which is constantly consumed by both dissipation and buoyancy. The Smagorinsky model, for example, is generally too dissipative for SBL simulations (Mason and Derbyshire 1990). As stability increases, spatially and temporally intermittent turbulence can develop and eddy sizes are strongly damped. If the SFS model cannot sustain intermittency, resolved turbulence will diminish quickly. This results in a false laminar flow field. Jiménez and Cuxart (2005) systematically explored the range of stable stratification that can be simulated with a TKE-based closure model. With a grid resolution of about 5 m, they were successful in simulating weakly and moderately stable conditions. Under strong stability, however, they reported runaway cooling, which is a result of the collapse of boundary layer turbulence.

Motivated by the difficulties in performing LES of the SBL, we attempt to relax the resolution requirement and, thus, extend the range of applicability of LES to strongly stable conditions, through better representation of SFS turbulence. The turbulence model used in this study is the dynamic reconstruction model (DRM) of Chow et al. (2005). The DRM has previously been shown to be advantageous in turbulent channel flow (Gullbrand and Chow 2003) and in neutral atmospheric boundary layer (ABL) simulations (Chow et al. 2005).

With a model setup similar to that for the GABLS case, we evaluate the performance of the DRM by first examining its ability to sustain resolved turbulence under moderate and strong atmospheric stability, with relatively coarse resolutions (section 4a). The quality of the coarse-resolution DRM simulations is checked by comparing mean turbulent statistics with flux-based surface similarity as well as high-resolution results. Simulations with other closures including the TKE-1.5 and the dynamic Wong–Lilly model are also performed to show the benefits of using the DRM closure. Furthermore, the SFS dissipation and backscatter of the turbulent kinetic energy is investigated (section 4b). The vertical structure of the SBL, including shear and turbulent Prandtl number, is examined using high-resolution simulations (sections 4c and 4d). The SFS representation with the DRM is analyzed through decomposition of heat flux and TKE (section 4e). Elevated TKE develops under the strongly stable setup in this LES study. Its intermittent nature is examined in section 4f. Finally, we examine the resolved flow structure with respect to different atmospheric stability and SFS parameterizations (section 4g).

The Advanced Regional Prediction System (ARPS) (Xue et al. 2000) is used for the simulations. ARPS is a nonhydrostatic mesoscale and small-scale LES finite difference model. The code has been adapted to accommodate the new DRM SFS closure using the explicit filtering and reconstruction framework (Chow and Street 2002; Chow 2004).

2. Explicit filtering and reconstruction framework

The traditional approach toward LES has been to treat the discrete differentiation operation as an implicit filter to separate large from small scales in the governing equations. With finite volume and finite difference approaches, implicit filtering can lead to truncation and aliasing errors due to the nonlinear terms (Lund 1997). Explicit filtering can minimize the influence of truncation errors and has been shown to be beneficial in recent studies (Lund 1997; Gullbrand 2001; Carati et al. 2001; Winckelmans et al. 2001; Gullbrand and Chow 2003).

In this study, a 3D explicit filter (a top-hat filter of width Δ_f twice the grid spacing) is applied to the Navier–Stokes equations and is treated separately from the numerical differencing operators. The implicit discretization operator is denoted by a tilde and the explicit filtering operator by a bar. In our notation, the tilde operator is a loose representation of the implicit filter operation, as its nature depends on the discrete differentiation schemes. The LES governing equations for the resolved fields are the momentum, continuity, and scalar transport equations:

$$\frac{\partial \bar{\rho}\,\tilde{\bar{u}}_i}{\partial t} + \frac{\partial \bar{\rho}\,\tilde{\bar{u}}_i \tilde{\bar{u}}_j}{\partial x_j} = -\frac{\partial \bar{p}}{\partial x_i} - \bar{\rho} g \delta_{i3} + \bar{\rho} \epsilon_{imn} f_n \tilde{\bar{u}}_m - \frac{\partial \bar{\rho} \tilde{\tau}_{ij}}{\partial x_j}, \tag{1}$$

$$\frac{\partial \bar{\rho}}{\partial t} + \frac{\partial \bar{\rho}\,\tilde{\bar{u}}_i}{\partial x_i} = 0, \tag{2}$$

and

$$\frac{\partial \tilde{\bar{\theta}}}{\partial t} + \frac{\partial \bar{\rho}\,\tilde{\bar{u}}_i \tilde{\bar{\theta}}}{\partial x_i} = -\frac{\partial \bar{\rho} \tilde{\chi}_i}{\partial x_i}, \tag{3}$$

where $\tilde{\bar{u}}_i$ are the velocity components, $\bar{p}$ the pressure, $\bar{\rho}$ the density, f the Coriolis parameter, and $\tilde{\bar{\theta}}$ the potential temperature. Further details are given in Chow (2004, appendixes C and D). The turbulent stresses and heat fluxes can be decomposed into resolvable subfilter-scale (RSFS) stresses and unresolvable subgrid-scale (SGS) stresses:

$$\tau_{ij} = \overline{u_i u_j} - \tilde{\bar{u}}_i \tilde{\bar{u}}_j = \underbrace{(\overline{u_i u_j} - \overline{\tilde{u}_i \tilde{u}_j})}_{\tau_{\mathrm{SGS}}} + \underbrace{(\overline{\tilde{u}_i \tilde{u}_j} - \tilde{\bar{u}}_i \tilde{\bar{u}}_j)}_{\tau_{\mathrm{RSFS}}} \tag{4}$$

and

$$\chi_i = \overline{u_i \theta} - \tilde{\bar{u}}_i \tilde{\bar{\theta}} = \underbrace{(\overline{u_i \theta} - \overline{\tilde{u}_i \tilde{\theta}})}_{\chi_{\mathrm{SGS}}} + \underbrace{(\overline{\tilde{u}_i \tilde{\theta}} - \tilde{\bar{u}}_i \tilde{\bar{\theta}})}_{\chi_{\mathrm{RSFS}}}. \tag{5}$$

The first set of parentheses on the rhs contains the SGS stresses τ_{SGS} and χ_{SGS}, which have scales finer than the grid resolution and, hence, must be modeled. The second set of parentheses contains the filtered-scale stresses τ_{RSFS} and χ_{RSFS}, which depend on the resolved and explicitly filtered velocity fields within the resolution domain. As the explicit filter function is well defined, it is theoretically possible to obtain $\tilde{u}_i$ from $\overline{\tilde{u}}_i$ and $\tilde{\theta}$ from $\overline{\tilde{\theta}}$ by deconvolution (inverse filtering). In this work, reconstruction is performed through the approximate deconvolution method (ADM) of van Cittert (1931) and Stolz et al. (2001):

$$\tilde{u}_i = \overline{\tilde{u}}_i + (I - G) * \overline{\tilde{u}}_i + (I - G) * [(I - G) * \overline{\tilde{u}}_i] + \cdots, \tag{6}$$

where I is the identity operator, G is the explicit filter, and asterisks denote the convolution operator. The RSFS term is computed by substituting the reconstructed velocity $\tilde{u}_i^*$ into the τ_{RSFS} term. Up to five levels of reconstruction are applied in this work to enhance the role of the RSFS stresses.

For subgrid-scale turbulence representation, we apply the Wong and Lilly (1994) dynamic eddy-viscosity model to represent SGS motions:

$$\tau_{SGS} = -2\nu_T \overline{\tilde{S}}_{ij}, \tag{7}$$

where $\overline{\tilde{S}}_{ij} = (\partial\overline{\tilde{u}}_i/\partial x_j + \partial\overline{\tilde{u}}_j/\partial x_i)/2$ is the resolved strain rate tensor and the dynamic eddy viscosity is given by $\nu_T = C_\epsilon \Delta^{4/3}$. The coefficient C_ϵ is determined using the least squares method of Lilly (1992). More details on the RSFS–SGS model can be found on Chow et al. (2005).

In the near-wall region, adjustments to the surface shear stress are necessary to improve LES performance near the surface (Brasseur and Wei 2010). We follow Chow et al. (2005), using a near-wall stress model to supplement the SGS stress based on the canopy stress model of Brown et al. (2001). Implementation of this near-wall model has proved successful in the work of Brown et al. (2001), Cederwall (2001), Chow et al. (2005), and Kirkpatrick et al. (2006).

The RSFS–SGS model framework can be viewed in terms of a mixed model (Bardina et al. 1983; Zang et al. 1993). The RSFS component is the so-called scale similarity term represented by reconstruction, and the SGS component is represented using an eddy-viscosity closure. The introduction of the RSFS terms decreases the required SGS contribution toward the total turbulent stresses. The original scale similarity model of Bardina et al. (1983) assumed that the smallest resolved scales possess a similar structure to the subfilter scales. The reconstruction model seeks a more accurate representation of the resolved scales by inverting the explicit filter operation. With higher levels of reconstruction, more details of high frequency motions approaching the grid cutoff are restored, thus improving the representation of the SFS stress. With zero-level reconstruction, the RSFS term reduces exactly to the scale similarity model of Bardina et al.

3. Model configuration

Simulations are performed on a (640 m × 640 m × 640 m) domain over flat but rough terrain, similar to that used in previous work (Kosovic and Curry 2000; Saiki et al. 2000; Basu and Porté-Agel 2006). Both anisotropic and isotropic grids for a range of spatial resolutions are used in this work (see Table 1). Vertical grid stretching is applied in the anisotropic runs to better resolve the surface layer. The finest spatial resolution used in this study is 3.125 m on a uniform grid. The GABLS intercomparison study suggested that LES results at this resolution are comparable to 2-m and 1-m resolution SBL simulations.

The lateral boundary conditions are periodic. Both the lower and upper boundary are set to be rigid walls. At the top boundary, Rayleigh damping is applied above 500 m. The boundary layer depth ranges from 100 to 200 m and therefore should not be affected by the Rayleigh damping. The surface momentum flux is prescribed by imposing Monin–Obukhov similarity at the first grid point above the ground:

$$U_s = \frac{u_*}{\kappa}\left[\ln\left(\frac{z + z_0}{z_0}\right) + \beta\frac{z}{L}\right], \quad L = -\frac{\theta_s}{g}\frac{u_*^3}{\kappa\overline{w\theta}_s}, \tag{8}$$

where U is the wind speed, u_* is the surface friction velocity, κ the von Kármán constant, and L the Obukhov length; surface quantities are subscripted s. In addition, β is a constant taken to be 4.7 from Businger et al. (1971), and z_0 is the surface roughness, set at 0.1 m. Both u and v have their surface values at $z = 0$. A displacement height equal to the roughness length has been added to the vertical coordinate.

The simulations are carried out at midlatitude (43.29°N) where the Coriolis parameter f is 1.00×10^{-4} s^{-1}. The flow is driven by a geostrophic wind at $(U_g, V_g) = (10 \text{ m s}^{-1}, 0 \text{ m s}^{-1})$ and initialized using a uniform wind profile with horizontal velocity components equal to the geostrophic velocities to avoid inertial oscillations in the upper part of the domain. The initial potential temperature is uniform at 300 K (neutral conditions). A random perturbation of 0.1 K is applied to the bottom 150 m of the domain at initialization to trigger turbulence.

TABLE 1. List of simulations and parameters: HR (VHR) denote high (very high) resolution. All cases use a surface heat flux of −0.02 K m s^{-1} unless specified with CR. Run names with an asterisk represent simulations with isotropic grid resolution. DWL is the dynamic Wong–Lilly model, and DRM is the dynamic reconstruction model. The 05CR-VHR* cases are driven by a surface cooling rate of −2.0 K h^{-1}.

Run	Grid size	Δx (m)	$\Delta z_{\min}$ (m)	Heat flux (K m s^{-1})	Reconstruction level
Smagorinsky	(43, 43, 43)	16	5	−0.02	N/A
TKE-02CR	(43, 43, 43)	16	5	−0.02	N/A
TKE-03CR	(43, 43, 43)	16	5	−0.03	N/A
TKE-04CR	(43, 43, 43)	16	5	−0.04	N/A
TKE-05CR	(43, 43, 43)	16	5	−0.05	N/A
TKE-07CR	(43, 43, 43)	16	5	−0.07	N/A
TKE-02CR-VHR*	(195, 195, 195)	3.125	3.125	−0.02	N/A
TKE-05CR-VHR*	(195, 195, 195)	3.125	3.125	−0.05	N/A
DWL	(43, 43, 43)	16	5	−0.02	N/A
DRM-ADM0	(43, 43, 43)	16	5	−0.02	0
DRM-ADM1	(43, 43, 43)	16	5	−0.02	1
DRM-ADM2	(43, 43, 43)	16	5	−0.02	2
DRM-02CR(DRM-ADM5)	(43, 43, 43)	16	5	−0.02	5
DRM-03CR	(43, 43, 43)	16	5	−0.03	5
DRM-04CR	(43, 43, 43)	16	5	−0.04	5
DRM-05CR	(43, 43, 43)	16	5	−0.05	5
DRM-07CR	(43, 43, 43)	16	5	−0.07	5
DRM-02CR-HR	(83, 83, 83)	8	2.5	−0.02	5
DRM-02CR-VHR*	(195, 195, 195)	3.125	3.125	−0.02	5
DRM-05CR-VHR*	(195, 195, 195)	3.125	3.125	−0.05	5

A constant surface heat flux is imposed on the bottom boundary to drive atmospheric cooling. In this study, five sets of surface heat flux (−0.02, −0.03, −0.04, −0.05, and −0.07 K m s^{-1}) are included. The strength of cooling is categorized based on the theoretical expression of Derbyshire (1990) for the minimum heat flux sustainable in a stable boundary layer:

$$\overline{w\theta}_{s,\min} = -\frac{\theta_s R_f}{g\sqrt{3}} G^2 |f|, \tag{9}$$

where G is the geostrophic wind speed and R_f is the flux Richardson number, a ratio of buoyancy destruction to shear production of TKE. The SBL is further categorized into regimes of continuous turbulence where R_f is below 0.25 (dynamically unstable); intermittent turbulence where R_f is between 0.25 and 1.0; and quiescent conditions where turbulence can no longer be sustained (dynamically stable). The two strongest cooling cases of this study (−0.05, −0.07 K m s^{-1}) fall into the intermittent turbulence regime. All cases are shown on the SBL stability chart in Fig. 1, where $B = -g/\theta_s \overline{w\theta}_s$ represents buoyancy destruction at the surface and two curves show R_f values of 1.0 and 0.25. Other LES studies of the SBL are also included in Fig. 1 for reference. Note that the Derbyshire expression is only used here to qualitatively determine the state of the SBL. The recent work of Sorbjan (2010) presented a more accurate estimate of the minimum sustainable heat flux, based on the vertical velocity variance σ_w and a temperature scale $T_w = N\sigma_w\theta_0/g$.

A buoyancy length scale is computed a posteriori to confirm that the resolution used in this study is adequate. We choose the Ozmidov scale $L_o = \epsilon^{-1/2}N^{-3/2}$ to represent the characteristic length scale of buoyancy, where ϵ is the dissipation rate and N is the buoyancy frequency. Dissipation is estimated by the net loss of energy from the resolved field. For moderate cooling cases (−0.02, −0.03 K m s^{-1}), Ozmidov scales of 7 and 5 m are found around the center of the SBL (z/h = 0.5, where h is the boundary layer depth). Therefore, grid resolution in the vertical direction is sufficient even on the coarse grids (5 m near the surface) for these two cooling cases due to grid stretching. For the stronger cooling cases, the Ozmidov scale decreases to less than 2 m. Thus, the turbulence closure models are relied on more heavily.

A summary of the simulation cases is listed in Table 1. Since this LES study focuses on the quasi-steady-state SBL, the simulation results presented in the following sections are restricted to the later period of the simulations when a quasi-steady state is achieved.

4. Simulation results

a. Sustained turbulence

All simulations are carried out for 50 000 s of physical time, with constant surface cooling. According to the GABLS study, a grid resolution of 6.25–12.5 m is

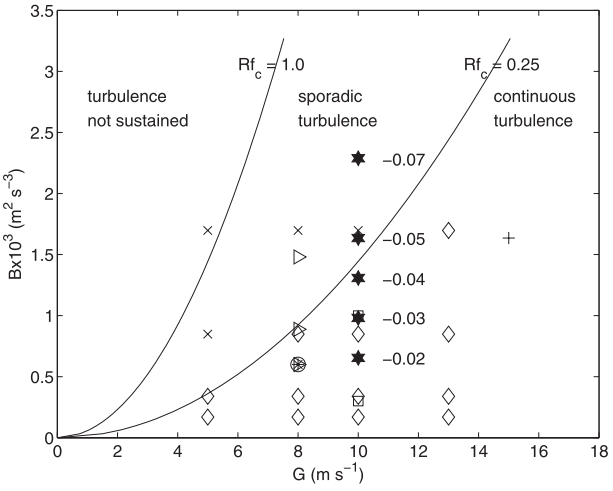

FIG. 1. Stability region of simulation cases: the horizontal axis represents geostrophic winds G and the vertical axis represents buoyancy $B = -g/\theta_s \overline{w\theta}_s$. Stars represent five levels of stability in this study, with surface heat flux (K m s^{-1}) noted on the right; open squares represent simulations by Mason and Derbyshire (1990), plus sign by Saiki et al. (2000), right-pointing arrow by Kosovic and Curry (2000), asterisk by Beare et al. (2006), small open circle by Basu and Porté-Agel (2006), diamonds by Jiménez and Cuxart (2005), and the multiplication sign is used for attempted cases that suffer from runaway cooling by Jiménez and Cuxart (2005).

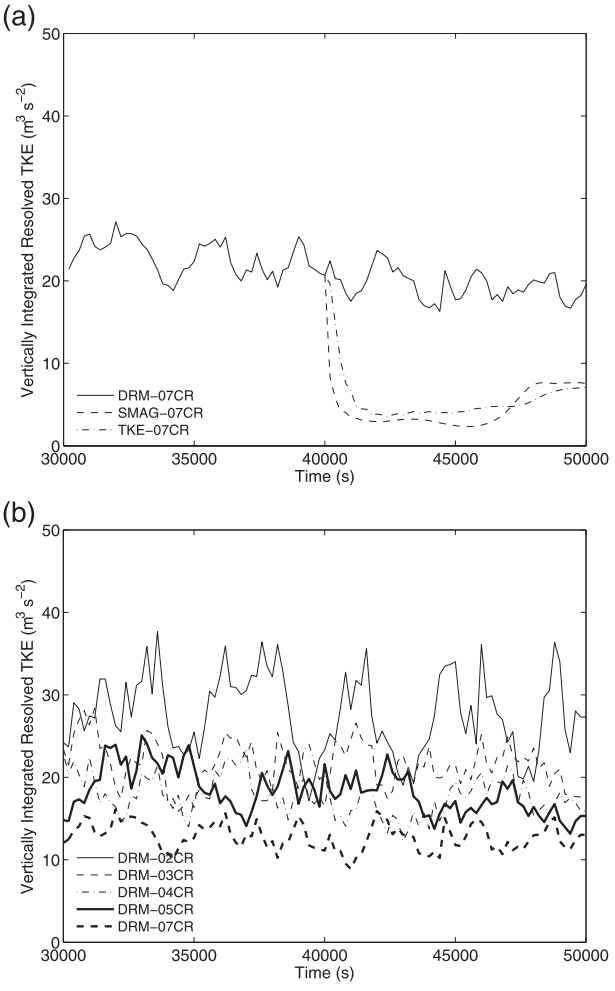

FIG. 2. Vertically integrated resolved TKE from 30 000 to 50 000 s for the (a) Smagorinsky, TKE-1.5, and DRM simulations starting from a turbulent initial state at 40 000 s under a strong surface cooling rate ($\overline{w\theta}_s = -0.07$ K m s^{-1}) and (b) DRM simulations under five surface cooling rates. Coarse-resolution results are presented.

required to sustain resolved turbulence under mild cooling for most turbulence models. In this study, the coarse-resolution simulations are performed on a grid with 16-m horizontal spacing and vertical stretching with 5-m spacing near the surface. The horizontal resolution used here is coarser than that of the GABLS study to test model performance. Note, however, that such resolution is still considered very high for current LES applications to real complex terrain (see, e.g., Michioka and Chow 2008).

First, we check if conventional closures can sustain resolved turbulence under the coarse resolutions used in this study. Simulations with the Smagorinsky model fail to generate resolved turbulence for moderate stability unless a spinup procedure is used to generate a convective atmospheric boundary layer as initial conditions. The TKE-1.5 simulations develop into a turbulent state with moderate cooling but produce laminar flow under strong stability, as do the Smagorinsky simulations. To confirm the role of proper SFS representation in preventing laminarization of the flow under strongly stable conditions, we also performed coarse-resolution simulations initialized from a turbulent field under strong stability. In Fig. 2a, time series of vertically integrated resolved TKE are presented as an indicator for resolved turbulence. Starting at 40 000 s from a DRM-generated flow field at strong stability, the Smagorinsky and TKE-1.5 simulations show rapid decay of resolved TKE. A small amount of resolved TKE is maintained afterward. In comparison, it is well sustained at roughly the same levels throughout the simulation with the DRM. Figure 2b shows resolved TKE from DRM simulations with different surface heat fluxes between 30 000 and 50 000 s. Decreases in both the mean value and magnitude of fluctuations are observed with stronger stability. Note that some wavelike patterns are visible in the TKE time series. The peaks are associated with energetic mixing events, which will be discussed in section 4f.

The quality of the simulations is also checked by computing the ratio of vertically integrated SFS TKE e to total TKE E as done in Jiménez and Cuxart (2005). For a fixed resolution, the e/E indicator must increase with stronger stability as the turbulent length scale

TABLE 2. Surface cooling rates calculated by a linear fit: e/E presents the percentage of vertically integrated SFS TKE divided by total TKE. Statistics are obtained using horizontally averaged values from 30 000 to 50 000 s.

Run	Heat flux (K m s^{-1})	Cooling rate (K h^{-1})	$e/E \times (100\%)$
DRM-02CR	−0.02	−0.410	68.8
DRM-03CR	−0.03	−0.667	71.0
DRM-04CR	−0.04	−1.07	71.9
DRM-05CR	−0.05	−1.14	74.4
DRM-07CR	−0.07	−1.98	76.8
TKE-02CR	−0.02	−0.410	47.4
TKE-03CR	−0.03	−1.08	**40.4**
TKE-04CR	−0.04	−2.45	**24.8**
TKE-05CR	−0.05	−4.32	**17.8**
TKE-07CR	−0.07	−10.8	**10.3**

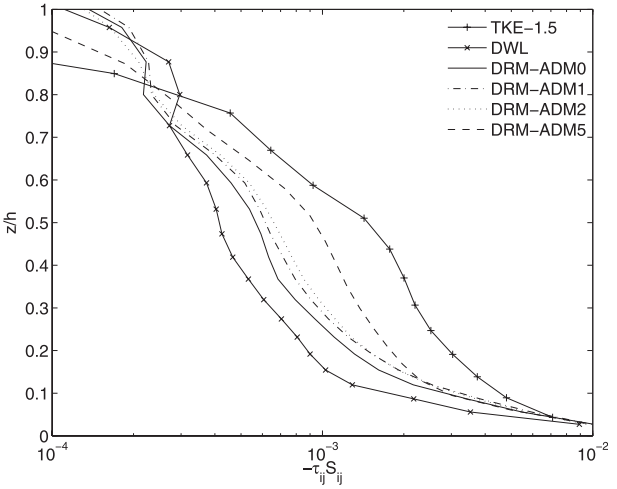

FIG. 3. Horizontally and time-averaged (last 7200 s) vertical profile of SFS dissipation from six closure models for the moderate stability case ($\overline{w\theta}_s = -0.02$ K m s^{-1}) The boundary layer depth h is ~160 m.

decreases. The values are computed by averaging over the last 20 000 s of simulation and are presented in Table 2. The monotonic increase of the ratio with stability further supports that turbulence is properly maintained for DRM simulations, while the TKE closure displays the opposite effect, indicating runaway cooling (highlighted in boldface). Note that the absolute percentages of the SFS TKE are larger than those obtained by Jiménez and Cuxart (2005). This is due to the unique property of the DRM closure in which part of the SFS terms originates from the resolved field. Further discussion is presented in section 4e.

In Table 2, the corresponding surface temperature drop with the TKE-1.5 simulations is much larger than with the DRM under the same surface heat flux for strong stability. This is because the TKE-1.5 closure is more dissipative than the DRM under stable conditions (see next subsection). Therefore, the TKE-1.5 simulations experience more limited turbulent mixing, resulting in shallower and colder boundary layers. Similar observations are also found in high-resolution simulations in which the TKE-1.5 and DRM simulations can end up in two very different states. For the purpose of comparing model performance under similar stability conditions for a strongly stable atmospheric boundary layer, the high-resolution TKE-1.5 (TKE-05CR-VHR*) and DRM (DRM-05CR-VHR*) simulations are driven by a constant surface temperature cooling rate of −2.0 K h^{-1} instead. This approach results in the same surface temperature and similar boundary layer depth—hence a similar vertical potential temperature gradient. The resulting surface heat flux at steady state is found to be around −0.05 K m s^{-1} for both cases.

b. SFS dissipation and backscatter

In this section, we proceed to show that the reason for the less stringent resolution requirements with the DRM is because it allows backscatter of SFS energy. In the TKE equation, the term $\Pi = -\tau_{ij}\overline{S}_{ij}$ represents energy transport between resolved and subfilter scales. It is called the SFS dissipation rate because it is mostly positive, indicating the transfer of energy from the resolved into the subfilter motions. But the reverse process, known as backscatter (negative Π values), also exists to feed back energy to the resolved scales, as confirmed in the field observations of Carper and Porté-Agel (2004).

Most canonical eddy-viscosity models are, however, purely dissipative by formulation. They tend to oversuppress turbulence development and cause flow to become laminar quickly under stable conditions (see section 4a). In contrast, scale similarity models naturally allow for backscatter, which is desirable for sustaining resolved turbulence in SBL simulations. In the DRM formulation, the RSFS stress is of the scale-similarity type. Therefore, the DRM includes backscatter, which is advantageous for simulations of the SBL.

Figure 3 compares the horizontally averaged SFS dissipation rate with that for the TKE-1.5, dynamic Wong–Lilly (DWL), and DRM models with four different levels of RSFS reconstruction. We observe that the reconstruction models are less dissipative than the TKE-1.5 model. Among the DRM results, Π increases with higher levels of reconstruction. This happens because eddies with higher wavenumbers toward the filter cutoff are restored under more reconstruction. Interactions between these relatively high wavenumber (small scale) motions are more likely to dissipate energy (Chow 2004). Note that the backscatter property is intrinsic to the reconstruction procedure and is different

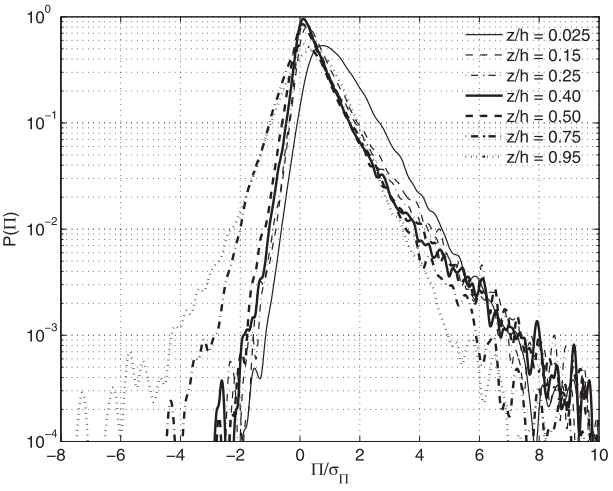

FIG. 4. Normalized probability density function $p(\Pi)$ at different vertical levels: case DRM-02CR.

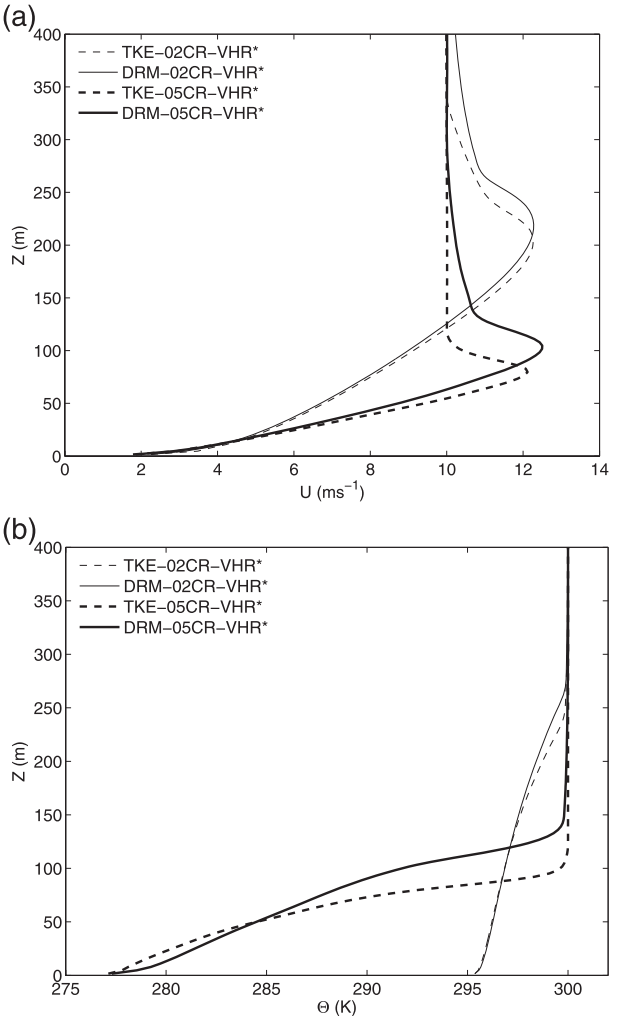

FIG. 5. Horizontally and time-averaged (last 7200 s) vertical profiles for (a) wind speed and (b) potential temperature for the moderate and strong stability cases.

from the stochastic backscatter type of LES models (Mason and Thomson 1992), in which random perturbations are added to the model domain to obtain correct near-wall behavior in the boundary layer.

In Fig. 3, the SFS dissipation (Π) for the DRM–ADM5 closure decreases with height, which could be due to either less dissipation or more backscatter. To investigate the source of the decrease we examine the probability density distribution of Π at different vertical elevations. Figure 4 plots the probability density function (PDF) of Π obtained over 1000 s using 20 samples at 50-s intervals (different sampling intervals and averaging periods show similar results). A Gaussian kernel density estimation method is used in computing the PDF. Following Carper and Porté-Agel (2004), Π is normalized by its standard deviation, in which case $P(\Pi)$ on the y axis is a dimensionless number. The overall shape of the PDF "swings" to the backscatter side with increasing height, showing more frequent backscatter events. The percentage backscatter calculated by counting the number of occurrences of negative Π is about 5% near the surface to roughly 35% approaching the top of the SBL.

c. *Vertical shear profiles*

Vertical profiles of mean wind speed and potential temperature at quasi-steady state from the 3.125-m-resolution simulations are plotted in Figs. 5a and 5b. A low-level jet (LLJ), located around the wind maximum, develops in all cases in Fig. 5a. The height of the wind maximum can be considered a measure for the SBL depth. The boundary layer depth is shallower under stronger stability, as expected due to more limited turbulent transport. For the same stability condition, the choice of turbulence models affects the depth of the boundary layer. The DRM produces a deeper SBL than for TKE-1.5 in both cases. The differences between the two closures are larger for strong stability (DRM 96 m, TKE 78 m) than for moderate stability (DRM 191 m, TKE 185 m). The dependence of SBL depth on the closure model is also documented in the GABLS study. It is interesting to note that the only two 1-m-resolution simulations of the GABLS study used a TKE-based model and a Smagorinsky model with stochastic backscatter. The latter produced a deeper (164 m) SBL than the former (149 m).

Monin–Obukhov (MO) similarity theory is used to test the performance of the simulations near the surface where the dimensionless height z/L is smaller than unity (Garratt 1992). Businger et al. (1971) experimentally obtained the following relationships for the SBL:

$$\phi_m = \frac{\kappa z}{u_*}\frac{\partial \overline{\tilde{U}}}{\partial z} = 1 + \beta\zeta; \quad \phi_h = \frac{\kappa z}{\theta_*}\frac{\partial \overline{\tilde{\theta}}}{\partial z} = 0.74 + \beta\zeta, \tag{10}$$

where ϕ_m and ϕ_h are the dimensionless wind shear and potential temperature gradient, $\zeta = z/L$ is the dimensionless height, β is a constant equal to the inverse of the critical gradient Richardson number Ri, and θ_* is a generic turbulent temperature scale defined as the ratio of surface heat flux to friction velocity.

Horizontally and time averaged dimensionless quantities are presented as a function of Ri in Fig. 6. Only the relevant ranges where MO similarity is valid (i.e., $z/L < 1$) are included in the plots. The dimensionless shear relationship is followed quite well for the DRM models in Fig. 6a, even at coarse resolution. In Fig. 6b, ϕ_h deviates from the Businger profile for small Richardson numbers. This could be due to the uncertainty in the surface Prandtl number, which is the intercept of Eq. (10) and is traditionally set at 0.74 (Grachev et al. 2007). Both the DRM and the TKE-1.5 runs are much better described by an intercept of 0.55 in Fig. 6b, which is the predicted surface Prandtl number in our simulations (see section 4d for further discussion).

The good agreement with MO similarity for level-5 reconstruction in DRM at coarse resolution is surprising since LES results at such resolutions are usually poor for conventional closures. The coarse-resolution simulations of DRM at four other reconstruction levels show improved agreement with surface similarity theory as levels of reconstruction increase. A similar finding is reported for LES of the neutral atmospheric boundary layer (Chow et al. 2005).

Although MO similarity theory provides a general guideline for surface flux scaling, it is much less certain that MO theory should apply under ''universal'' stable conditions, particularly under strong stability (Sorbjan 2006). Sorbjan and Grachev (2010), and Sorbjan (2010) introduced gradient-based scaling, which is applicable in a wider stability range. Therefore, the master scaling of Sorbjan (2010) is also used to examine the quality of the simulations:

$$\frac{\tau}{U_s^2} = \frac{1}{\mathrm{Ri}(1 + 300\mathrm{Ri}^2)^{3/2}};$$
$$\frac{-\overline{w\theta}}{U_s T_s} = \frac{1}{0.9\mathrm{Ri}^{1/2}(1 + 250\mathrm{Ri}^2)^{3/2}}, \tag{11}$$

where $U_s = \kappa z N$ and $T_s = \kappa z d\theta/dz$. The numerical coefficients were obtained using data from the Surface Heat Budget of the Arctic Ocean (SHEBA) field program in the Arctic (Sorbjan 2010). Figures 7a and 7b present statistics obtained from the 3.125-m simulations using the TKE-1.5 and DRM models. Results from both closures support the gradient-based formulation at moderate stability very well. For strong stability, the agreement is quite good. The TKE-1.5 results are slightly better for smaller Ri, while the DRM is better for larger Ri values. Even higher resolution simulations are likely needed for better comparison under strong stability.

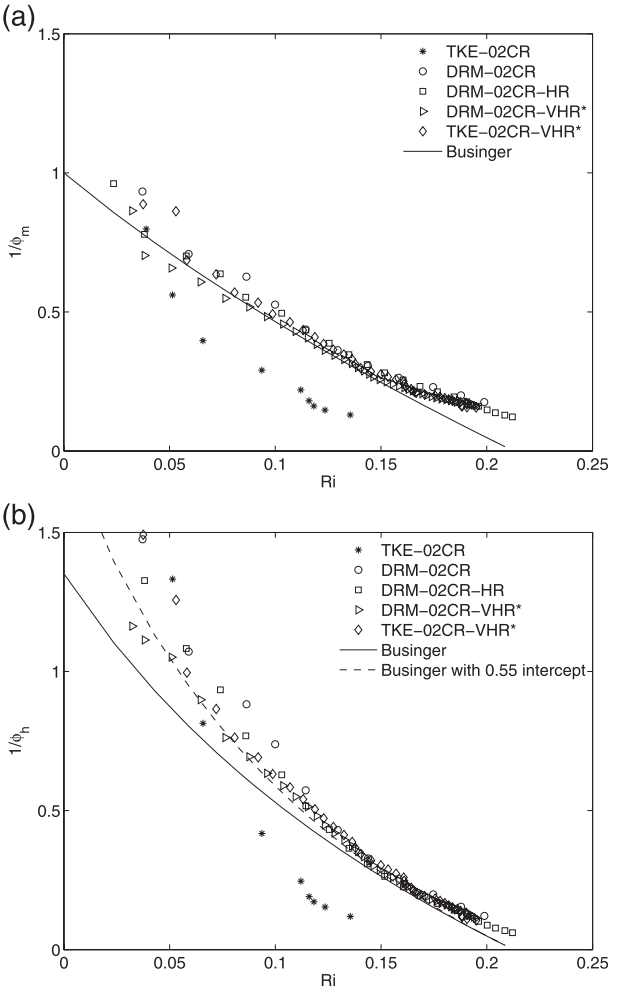

FIG. 6. Horizontally and time-averaged (last 7200 s) inverse nondimensional (a) shear and (b) temperature gradient for the moderate stability case. Both dimensionless quantities are limited to $z/L < 1$. They are plotted as a function of gradient Richardson number and compared to MO similarity theory.

d. Turbulent Prandtl number

In the previous section, we noted that under moderate stability agreement with the dimensionless potential temperature gradient near the surface can be improved by choosing 0.55 as the turbulent Prandtl number Pr_T in the MO formulation. This conclusion is not limited to

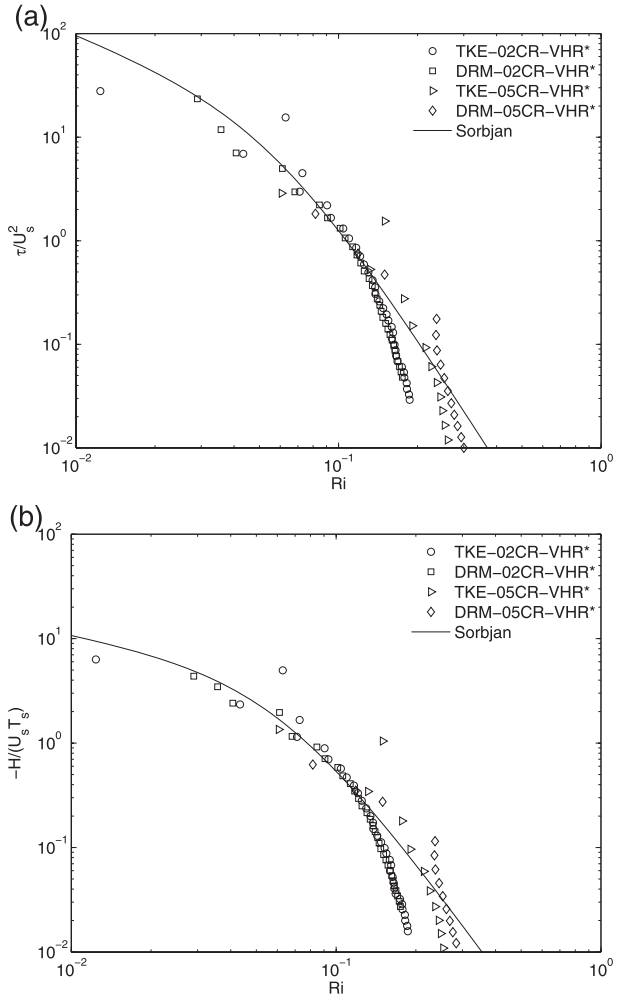

FIG. 7. Horizontally and time-averaged (last 7200 s) nondimensional (a) shear and (b) temperature gradient for the moderate and strong stability cases. Both dimensionless quantities are limited to $z/L < 1$ and are plotted as a function of gradient Richardson number and compared to the gradient-based scaling.

the DRM closures but is also true for TKE-1.5 closure at 3.125-m resolution (see Fig. 6b). The Pr_T represents the relative efficiency of turbulent mixing for momentum versus heat. It is an important dimensionless number for flux parameterization in the SBL (Gerz et al. 1989) and is usually prescribed as a stability-dependent constant for LES with the Smagorinsky or TKE-1.5 closures. The variation of the Prandtl number in the SBL can be described using the formulation proposed by Schumann and Gerz (1995) for equilibrium flows:

$$\mathrm{Pr}_T = \mathrm{Pr}_{T0} \exp\left(-\frac{\mathrm{Ri}}{\mathrm{Pr}_{T0}\mathrm{Ri}_\infty}\right) + \frac{\mathrm{Ri}}{\mathrm{Ri}_\infty}, \qquad (12)$$

where Pr_{T0} is a surface value and Ri_∞ is a constant gradient Richardson number limit in the SBL. Nieuwstadt (1984) hypothesized a constant value of 0.2 for Ri in the SBL as part of the "z-less" scaling hypothesis, which we adopt for the above formulation as Ri_∞.

Since LES with the DRM models independently predicts momentum and heat fluxes (Pr_T is not prescribed in advance) that agree well with similarity theory, the variation of Pr_T in the SBL can be quantified. As shown in Fig. 8, Ri remains nearly constant at 0.2 from around $z/h > 0.4$ to the top of the SBL. A remarkably good fit with the Schumann and Gerz formulation is observed for Pr_T until 70% of the boundary layer depth. The Pr_T values for higher cooling cases show a similar pattern and agreement, with slightly different Pr_{T0}, and Ri_∞ values; for example, $\mathrm{Pr}_{T0} = 0.4$ and $\mathrm{Ri}_\infty = 0.25$ gives the best fit for the case where $\overline{w\theta}_s = -0.03\,\mathrm{K\ m\ s^{-1}}$ (not shown). The DRM results show that Pr_T exceeds unity approaching the top of the boundary layer, as the Richardson number increases. While this is allowed by Eq. (12), it contradicts the gradient-based scaling in Eq. (11). Whether Pr_T can exceed 1 in the SBL is still a debated issue. Readers are referred to Grachev et al. (2007) for a more comprehensive discussion.

e. Turbulent flux decomposition

The role of reconstruction in the DRM is investigated by comparing the resolved and subfilter-scale turbulent fluxes from the DRM with the standard TKE-1.5 closure. Figure 9 presents the horizontally averaged heat flux for the moderate cooling case. The total heat flux is nearly identical for both closures. The DRM has a larger SFS component and a smaller resolved component than does the TKE-1.5 model. This is due to the presence of the RSFS stress, which is extracted from the resolved field and is included in the SFS component of the model. The resolved stress is reduced accordingly.

The presence of the resolved subfilter-scale stresses allows us to directly compute SFS TKE. This is a unique property that many eddy-viscosity closures (such as the Smagorinsky model) do not have, since the sum of the trace of the stress tensor τ_{kk} is zero, and therefore a model must be used to estimate SFS TKE if needed. For the DRM, however, τ_{kk} is nonzero because of the RSFS part. Using Taylor series expansions, it can be shown that $\tau_{\mathrm{RSFS},kk}$ is a function of the sum of the squares of the velocity gradients multiplied by the filter width squared plus higher order terms. For example, the level-0 reconstructed stresses $\tau_{\mathrm{RSFS},kk}$ for an isotropically filtered field can be expressed as

$$\tau_{\mathrm{RSFS},kk} = \overline{\bar{\bar{u}}_k \bar{\bar{u}}_k} - \bar{\bar{u}}_k \bar{\bar{u}}_k = \frac{\Delta^2}{12} \overline{\frac{\partial \bar{\bar{u}}_k}{\partial x_j} \frac{\partial \bar{\bar{u}}_k}{\partial x_j}} + O(\Delta^4), \qquad (13)$$

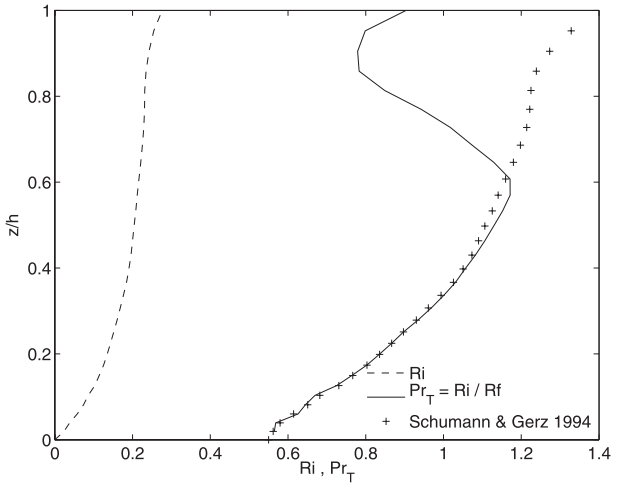

FIG. 8. Horizontally and time-averaged (last 7200 s) vertical profiles of turbulent Prandtl number and gradient Richardson number for the moderate cooling case ($\overline{w\theta}_s = -0.02\,\mathrm{K\ m\ s^{-1}}$) compared to the theory of Schumann and Gerz (1995).

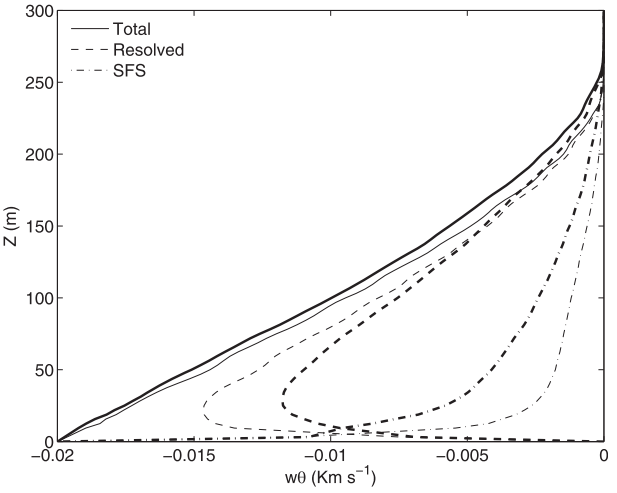

FIG. 9. Comparison of horizontally and time-averaged (last 7200 s) heat flux components of the DRM-02CR-VHR* (thick lines) and TKE-02CR-VHR* (thin lines) for the moderate stability case ($\overline{w\theta}_s = -0.02\,\mathrm{K\ m\ s^{-1}}$).

where Δ is the explicit filter width (see Chow 2004, appendix A). Similar to heat flux, the vertical profiles of the total TKE from the DRM and the TKE-1.5 closure are similar, with different partitioning of resolved/SFS components. This suggests that the DRM does offer a reliable direct measure of SFS TKE. In the present study of the SBL, it does so mostly by accounting for the vertical gradients in the filtered horizontal velocity field $(\overline{\tilde{u}}, \overline{\tilde{v}})$.

f. Low-level jet and elevated TKE

In a classical SBL, turbulence is generated at the surface and transported upward. In a nonclassical SBL, turbulence can also be generated aloft due to strong shear above and below the low-level jet. This TKE generation mechanism is referred to as the turbulence and mean shear interactions by Nakamura and Mahrt (2005). In the numerical simulation literature, elevated TKE was previously simulated by Conangla and Cuxart (2006) and Cuxart and Jiménez (2007).

The mean vertical shear profile for moderate and strong stability is presented in Fig. 10 for the DRM results at 3.125-m resolution. At the high cooling rate, mean shear increases significantly within the SBL. This increase of shear is due to the decrease in the boundary layer depth h. Furthermore, the shear strength also greatly increases above the jet nose. As the mean shear strengthens, greater amounts of mechanical production of TKE can be expected. The rate of TKE growth or decay, however, must be evaluated by also considering the buoyancy destruction process. In Fig. 10, the vertical potential temperature gradient shows a local maximum above the top of the boundary layer, which presents a severe limit to turbulent mixing processes. Although shear increases both below and above the jet, turbulent bursting events are more likely to occur in the subjet region.

The presence of TKE in the subjet region is identified by looking at time series of point measurements at different elevations in the SBL. The turbulent kinetic energy in Fig. 11 is computed by $e = 1/2(u'^2 + v'^2 + w'^2)$, where u', v', and w' are the fluctuating components of time-detrended velocities, to represent what might be seen at a meteorological tower with sonic anemometers

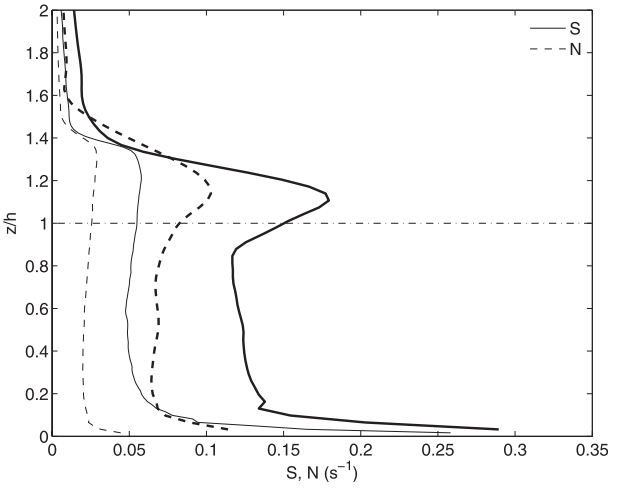

FIG. 10. Horizontally and time-averaged (last 7200 s) vertical profiles of mean shear $S = (du/dz^2 + dv/dz^2)^{1/2}$ and buoyancy frequency $N = [(g/\theta)d\theta/dz]^{1/2}$: thin lines represent the moderate stability case ($\overline{w\theta}_s = -0.02\mathrm{K\ m\ s^{-1}}$), and thick lines represent the strong stability case ($\overline{w\theta}_s = -0.05\,\mathrm{K\ m\ s^{-1}}$). The dashed–dotted line shows the dimensionless SBL height $z/h = 1$.

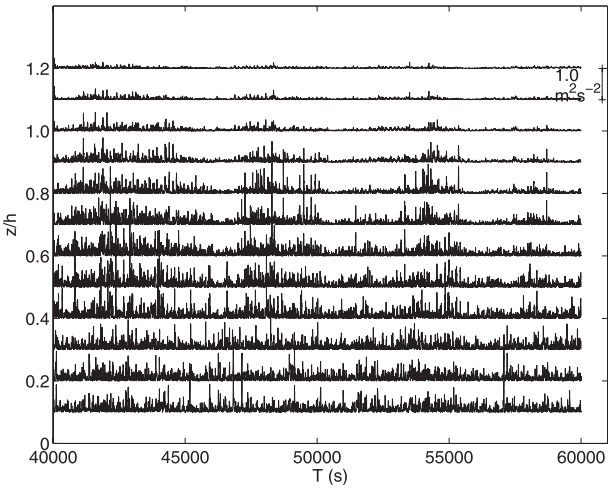

FIG. 11. Time series of $e = 1/2(u'^2 + v'^2 + w'^2)$ at different elevations for the strong stability case DRM-05CR-VHR* ($\overline{w\theta}_s = -0.05\,\mathrm{K\ m\ s^{-1}}$).

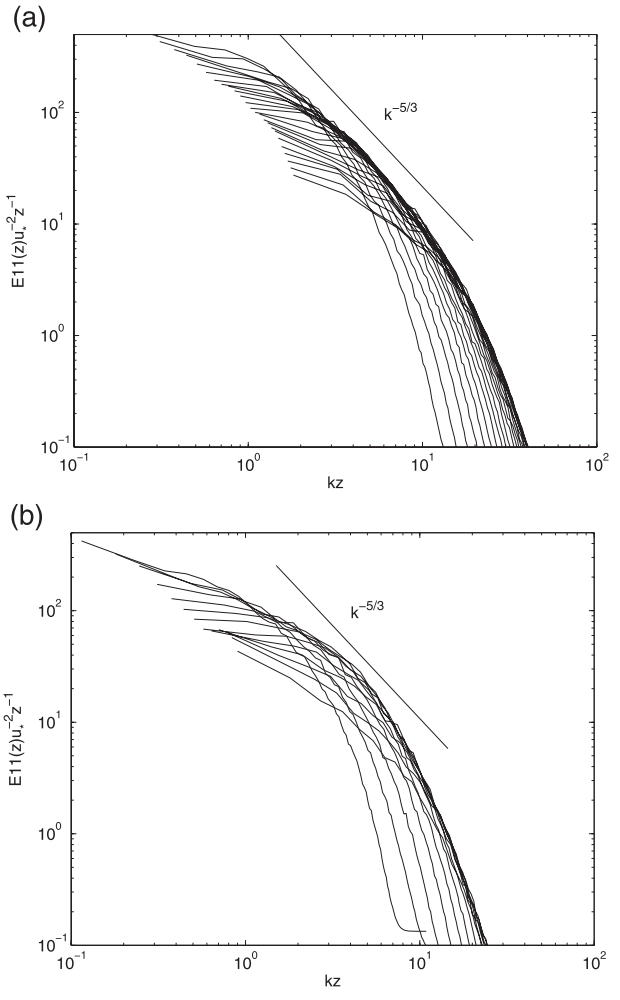

FIG. 12. Normalized one-dimensional energy spectrum for (a) DRM-02CR-VHR* and (b) DRM-05CR-VHR*. Each curve is a different height above the wall, starting at the left at $z/h = 0.1$ up to $z/h = 0.9$. All spectra are time averaged from 40 000 to 50 000 s.

at different heights. We observe extended periods where e is suppressed under strong stability conditions. This is more significant at higher elevations toward the LLJ nose at 100 m ($z/h = 1$). In between the quiescent periods, large increases of e over a relatively short time scale are present. Therefore, the nature of the elevated TKE appears intermittent. Quantitatively, intermittency can be measured by sorting a turbulent quantity in descending order according to its absolute magnitude and then counting the fraction of time that makes up the first 50% of the total time-integrated quantity. This is adapted from the intermittency definition by Coulter and Doran (2002) using heat flux as the turbulence indicator. In the continuous limit, this fraction will be 0.5, meaning that 50% of the total quantity is achieved in 50% of the total time. Here, the fraction computed for e is found to be 25% at 80 m ($z/h = 0.8$), which confirms the intermittent nature of the elevated TKE.

g. Spectra and velocity structure

Figure 12 shows the one-dimensional energy spectra of the streamwise velocity $\overline{\tilde{u}}$ at different heights within the SBL. Time-averaged data from each height are used to generate the spectra for the moderate and strong stability cases. The scaling procedure of Perry et al. (1986) and Porté-Agel et al. (2000) is adopted to collapse the data. A limited inertial subrange region is present in a small region of the energy spectra for the moderate case. For the stronger stability case, the presence of the inertial subrange is hard to identify. Considering the Ozmidov scale in the center depth of the boundary layer to be 2 m in this case, even higher resolution than 3.125 m may be needed to fully resolve the turbulence in the SBL, though finite difference errors will always tend to limit the extent of the inertial subrange.

The flow structure is of practical importance for studying scalar transport and dispersion processes in the atmospheric boundary layer. The structure of the resolved flow is sensitive to the SFS parameterization, and large differences are usually found in the near-surface layers (Ludwig et al. 2009). The variability of flow with the TKE-1.5 and DRM closures is examined from contour plots of the instantaneous streamwise velocity in the horizontal plane at 20 m above the surface, as shown in Fig. 13. Under moderate stability, velocity contours of the TKE-1.5 and DRM closures are similar. The size of the fluctuations qualitatively shows the limited eddy sizes in the SBL. Under strong stability, differences are observed between the two closures. The TKE-1.5 model reveals banded streaklike structures aligned with the

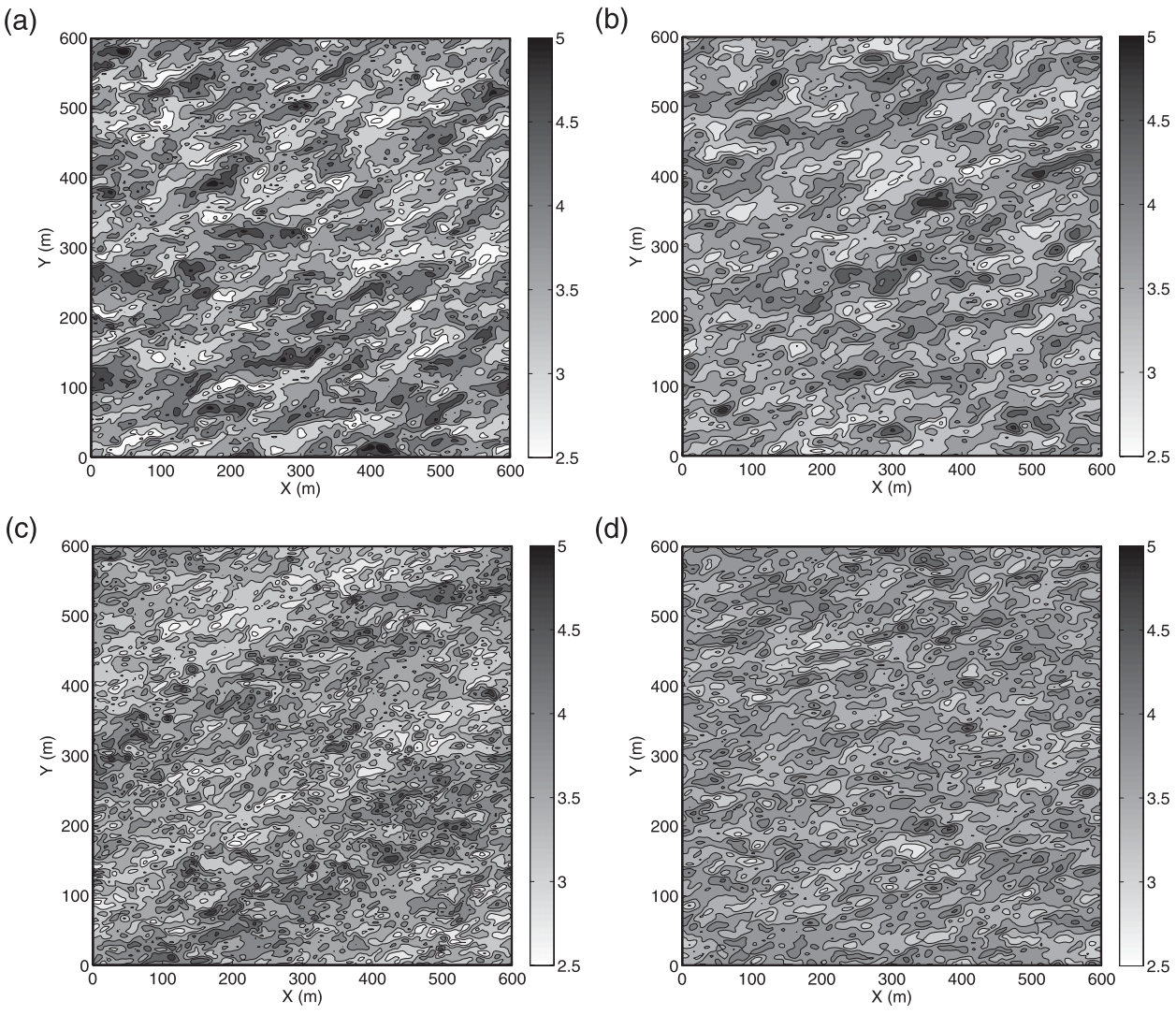

FIG. 13. Contours of instantaneous u velocity in the horizontal plane at around 20 m above the surface for the (top) moderate and (bottom) strong stabilities simulated with the (left) TKE-1.5 and (right) DRM closures: (a) TKE-02CR-VHR*, (b) DRM-02CR-VHR*, (c) TKE-05CR-VHR*, and (d) DRM-05CR-VHR*.

mean wind vector near the surface. Such a pronounced linear extent of the TKE-1.5 closure has been observed in other studies (Ludwig et al. 2009; Mirocha et al. 2010) for the neutral atmospheric boundary layer. In comparison, the DRM predicts a more realistic flow structure without any banded patterns. The eddy sizes are much smaller in the DRM simulations corresponding to the more limited turbulent length scale.

5. Summary

This study performed LES of the stably stratified atmospheric boundary layer using the explicit filtering framework and dynamic reconstruction turbulence model of Chow et al. (2005). With constant geostrophic forcing and prescribed surface cooling, a quasi-steady-state SBL was simulated with sustained turbulence, at coarser resolutions than typically recommended for SBL simulations, even under strong cooling scenarios. The DRM is capable of capturing atmospheric dynamics, for example the proper representation of SFS backscatter, that do not conform to traditional assumptions of gradient-diffusion turbulence models. The net energy drain from the resolved fields is therefore reduced to prevent the false laminarization problem experienced by other conventional eddy-viscosity closures. The probability distribution of dissipation reveals increased percentage backscatter with height, confirming the importance for choosing SFS models that have some backscatter component for SBL simulation purposes.

Compared with the TKE-1.5 closure, we found that the dynamic reconstruction model improves the representation of MO surface similarity under moderate stability even at coarse resolutions (e.g., 16-m horizontal spacing). The improvement was shown to be a result of higher levels of reconstruction, which increasingly restores turbulent scales near the filter cutoff. Overall, the DRM's ability to sustain turbulence and better represent mean shear and potential temperature gradient profiles at coarse resolution opens up possibilities for performing LES over real complex terrain under stable conditions, where spatial resolution is usually more limited than in idealized SBL studies.

High-resolution simulations were used to investigate the flow structure and turbulent statistics of the SBL. General agreement with the Businger–Dyer flux-based similarity is observed in the surface layer. The LES results also support the gradient-based similarity formulation of Sorbjan (2010), although results at strong stability likely require even higher resolution simulations. The turbulent Prandtl number calculated from DRM closures supports the formulation of Schumann and Gerz (1995). This suggests the use of a Richardson number–based turbulent Prandtl number formulation for SBL simulations.

Flux decomposition was used to show the unique feature of the DRM to include the RSFS component. The DRM allows direct prediction of the SFS TKE. Comparison with the TKE-1.5 model showed that this is a reliable measure. The presence of elevated TKE below the low-level jet was also described. This is a result of increased shear in the subjet region. This elevated TKE is shown to be intermittent in nature. Finally, spectra and near-surface velocity contours were presented. Under strong stability, the TKE-1.5 closure shows banded streak structures, which is likely unrealistic. The flow structures from the DRM are more reliable, as they become finer as stability increases without developing any correlated structures in the flow direction.

We have demonstrated the ability of explicit filtering and dynamic reconstruction models to successfully simulate the boundary layer under stable conditions. LES with DRM is capable of covering a wide range of stability conditions, extending into the intermittent turbulence regime where traditional LES closures usually fail. The approach described has the advantage that almost any existing SGS model can be adapted to an explicit filtering and reconstruction framework. This is achieved most simply by adding a scale similarity component (RSFS) to existing SGS closures (see Chow and Street 2009; Chow et al. 2005). The present study provides a promising outlook for the success of future LESs applied to real terrain under stable conditions.

Acknowledgments. We are grateful for support from National Science Foundation Grant ATM- 0645784 (Physical and Dynamic Meteorology Program). Acknowledgment is also made to the National Center for Atmospheric Research, which is sponsored by NSF, for the computing time used in this research.

REFERENCES

Bardina, J., J. Ferziger, and W. Reynolds, 1983: Improved turbulence models based on large eddy simulation of homogeneous, incompressible, turbulent flows. Dept. of Mechanical Engineering Tech. Rep. TF-19, Stanford University, 97 pp.

Basu, S., and F. Porté-Agel, 2006: Large-eddy simulation of stably stratified atmospheric boundary layer turbulence: A scale-dependent dynamic modeling approach. *J. Atmos. Sci.,* **63,** 2074–2091.

Beare, R., and Coauthors, 2006: An intercomparison of large-eddy simulations of the stable boundary layer. *Bound.-Layer Meteor.,* **118,** 247–272.

Brasseur, J. G., and T. Wei, 2010: Designing large-eddy simulation of the turbulent boundary layer to capture law-of-the-wall scaling. *Phys. Fluids,* **22,** 021303, doi:10.1063/1.3319073.

Brown, A., J. Hobson, and N. Wood, 2001: Large-eddy simulation of neutral turbulent flow over rough sinusoidal ridges. *Bound.-Layer Meteor.,* **98,** 411–441.

Businger, J., J. Wyngaard, Y. Izumi, and E. Bradley, 1971: Flux-profile relationships in atmospheric surface layer. *J. Atmos. Sci.,* **28,** 181–189.

Carati, D., G. Winckelmans, and H. Jeanmart, 2001: On the modelling of the subgrid-scale and filtered-scale stress tensors in large-eddy simulation. *J. Fluid Mech.,* **441,** 119–138.

Carper, M., and F. Porté-Agel, 2004: The role of coherent structures in subfilter-scale dissipation of turbulence measured in the atmospheric surface layer. *J. Turbul.,* **5,** 040, doi:10.1088/1468-5248/5/1/040.

Cederwall, R. T., 2001: Large-eddy simulation of the evolving boundary layer over flat terrain. Ph.D. thesis, Stanford University, 231 pp.

Chow, F. K., 2004: Subfilter-scale turbulence modeling for large-eddy simulation of the atmospheric boundary layer over complex terrain. Ph.D. thesis, Stanford University, 339 pp.

——, and R. L. Street, 2002: Modeling unresolved motions in les of field-scale flows. Preprints, *15th Symp. on Boundary Layer and Turbulence,* Wageningen, Netherlands, Amer. Meteor. Soc., 9.5. [Available online at http://ams.confex.com/ams/pdfpapers/44769.pdf.]

——, and ——, 2009: Evaluation of turbulence closure models for large-eddy simulation over complex terrain: Flow over Askervein Hill. *J. Appl. Meteor. Climatol.,* **48,** 1050–1065.

——, ——, M. Xue, and J. Ferziger, 2005: Explicit filtering and reconstruction turbulence modeling for large-eddy simulation of neutral boundary layer flow. *J. Atmos. Sci.,* **62,** 2058–2077.

Conangla, L., and J. Cuxart, 2006: On the turbulence in the upper part of the low-level jet: An experimental and numerical study. *Bound.-Layer Meteor.,* **118,** 379–400.

Coulter, R., and J. Doran, 2002: Spatial and temporal occurrences of intermittent turbulence during CASES-99. *Bound.-Layer Meteor.,* **105,** 329–349.

Cuxart, J., and M. A. Jiménez, 2007: Mixing processes in a nocturnal low-level jet: An LES study. *J. Atmos. Sci.,* **64,** 1666–1679.

Derbyshire, S., 1990: Nieuwstadt stable boundary-layer revisited. *Quart. J. Roy. Meteor. Soc.,* **116A,** 127–158.

Garratt, J. R., 1992: *The Atmospheric Boundary Layer*. Cambridge University Press, 316 pp.

Gerz, T., U. Schumann, and S. Elghobashi, 1989: Direct numerical simulation of the stratified homogeneous turbulent shear flows. *J. Fluid Mech.,* **200,** 563–594.

Grachev, A. A., E. L Andreas, C. W. Fairall, P. S. Guest, and P. O. G. Persson, 2007: On the turbulent Prandtl number in the stable atmospheric boundary layer. *Bound.-Layer Meteor.,* **125,** 329–341.

Gullbrand, J., 2001: Explicit filtering and subgrid-scale models in turbulent channel flow. Annual Research Briefs, Center for Turbulence Research, NASA Ames–Stanford University, 31–42.

——, and F. Chow, 2003: The effect of numerical errors and turbulence models in large-eddy simulations of channel flow, with and without explicit filtering. *J. Fluid Mech.,* **495,** 323–341.

Jiménez, M., and J. Cuxart, 2005: Large-eddy simulations of the stable boundary layer using the standard Kolmogorov theory: Range of applicability. *Bound.-Layer Meteor.,* **115,** 241–261.

Kirkpatrick, M., A. Ackerman, D. Stevens, and N. Mansour, 2006: On the application of the dynamic Smagorinsky model to large-eddy simulations of the cloud-topped atmospheric boundary layer. *J. Atmos. Sci.,* **63,** 526–546.

Kosovic, B., and J. Curry, 2000: A large eddy simulation study of a quasi-steady, stably stratified atmospheric boundary layer. *J. Atmos. Sci.,* **57,** 1052–1068.

Lilly, D. K., 1992: A proposed modification of the Germano subgrid-scale closure method. *Phys. Fluids,* **4A,** 633–635.

Ludwig, F. L., F. K. Chow, and R. L. Street, 2009: Effect of turbulence models and spatial resolution on resolved velocity structure and momentum fluxes in large-eddy simulations of neutral boundary layer flow. *J. Appl. Meteor. Climatol.,* **48,** 1161–1180.

Lund, T. S., 1997: On the use of discrete filters for large eddy simulation. Annual Research Briefs, Center for Turbulence Research, NASA Ames–Stanford University, 83–95.

Mason, P., and S. Derbyshire, 1990: Large-eddy simulation of the stably stratified atmospheric boundary-layer. *Bound.-Layer Meteor.,* **53,** 117–162.

——, and D. Thomson, 1992: Stochastic backscatter in large-eddy simulations of boundary-layers. *J. Fluid Mech.,* **242,** 51–78.

Michioka, T., and F. K. Chow, 2008: High-resolution large-eddy simulations of scalar transport in atmospheric boundary layer flow over complex terrain. *J. Appl. Meteor. Climatol.,* **47,** 3150–3169.

Mirocha, J. D., J. K. Lundquist, and B. Kosovic, 2010: Implementation of a nonlinear subfilter turbulence stress model for large-eddy simulation in the Advanced Research WRF model. *Mon. Wea. Rev.,* **138,** 4212–4228.

Nakamura, R., and L. Mahrt, 2005: A study of intermittent turbulence with CASES-99 tower measurements. *Bound.-Layer Meteor.,* **114,** 367–387.

Nieuwstadt, F., 1984: The turbulent structure of the stable, nocturnal boundary-layer. *J. Atmos. Sci.,* **41,** 2202–2216.

Perry, A., S. Henbest, and M. Chong, 1986: A theoretical and experimental-study of wall turbulence. *J. Fluid Mech.,* **165,** 163–199.

Porté-Agel, F., M. Parlange, C. Meneveau, W. Eichinger, and M. Pahlow, 2000: Subgrid-scale dissipation in the atmospheric surface layer: Effects of stability and filter dimension. *J. Hydrometeor.,* **1,** 75–87.

Saiki, E., C. Moeng, and P. Sullivan, 2000: Large-eddy simulation of the stably stratified planetary boundary layer. *Bound.-Layer Meteor.,* **95,** 1–30.

Schumann, U., and T. Gerz, 1995: Turbulent mixing in stably stratified shear flows. *J. Appl. Meteor.,* **34,** 33–48.

Sorbjan, Z., 2006: Local structure of turbulence in stably stratified boundary layers. *J. Atmos. Sci.,* **63,** 1526–1537.

——, 2010: Gradient-based scales and similarity laws in the stable boundary layer. *Quart. J. Roy. Meteor. Soc.,* **136A,** 1243–1254.

——, and A. A. Grachev, 2010: An evaluation of the flux-gradient relationship in the stable boundary layer. *Bound.-Layer Meteor.,* **135,** 385–405.

Stolz, S., N. Adams, and L. Kleiser, 2001: The approximate deconvolution model for large-eddy simulations of compressible flows and its application to shock-turbulent-boundary-layer interaction. *Phys. Fluids,* **13,** 2985–3001.

van Cittert, P., 1931: Der spaltbreite auf die intensitasverteilung in spektrallinien ii. *Z. Phys.,* **69,** 298–308.

Winckelmans, G., A. Wray, O. Vasilyev, and H. Jeanmart, 2001: Explicit-filtering large-eddy simulation using the tensor-diffusivity model supplemented by a dynamic Smagorinsky term. *Phys. Fluids,* **13,** 1385–1403.

Wong, V., and D. Lilly, 1994: A comparison of 2 dynamic subgrid closure methods for turbulent thermal-convection. *Phys. Fluids,* **6,** 1016–1023.

Xue, M., K. Droegemeier, and V. Wong, 2000: The Advanced Regional Prediction System (ARPS)—A multi-scale nonhydrostatic atmospheric simulation and prediction model. Part I: Model dynamics and verification. *Meteor. Atmos. Phys.,* **75,** 161–193.

Zang, Y., R. Street, and J. Koseff, 1993: A dynamic mixed subgrid-scale model and its application to turbulent recirculation-flows. *Phys. Fluids,* **5A,** 3186–3196.